DIGITAL IMAGE CORRELATION ANALYSIS FOR COMPRESSION AFTER IMPACT CHARACTERIZATION OF COMPOSITE PANELS

Dondish, A.[1], Li, L.[2], Melenka, G.W.[1]*
[1] Department of Mechanical Engineering, Lassonde School of Engineering, York University, North York, Canada
[2] Aerospace Research Centre, National Research Council of Canada, Ottawa, Canada
* Corresponding author (gmelenka@yorku.ca)

Abstract

Conventional strain measurement techniques such as strain gauge measurement typically do not offer sufficient information related to the complex responses of carbon fibre reinforced polymer (CFRP) composite panels subjected to dynamic loading. This work investigates CFRP panels in compression after impact (CAI) testing under varying boundary conditions, through additional support plates, using a full-field three-dimensional digital image correlation (3D DIC) technique. As part of a larger study conducted with different levels of impact energies, this study focuses on damage scenarios with 75 Joule (J) of impact energy. Out-of-plane displacement measurements from 3D DIC on each face of the impacted panels demonstrated the effects of the boundary conditions on local and global buckling behaviours. Axial strain measurements demonstrated the effects of the damaged region on the local strain distribution and allowed for an estimation of compressive material properties. Comparison of localized strain measurements from "virtual strain gauges" with those from conventional strain gauges demonstrated the measurement errors near expected values.

Keywords*: three-dimensional digital image correlation, compression after impact, out-of-plane displacement field*

1 Introduction

Fibre-reinforced polymer matrix composite materials are used in the aerospace industry for their favourable properties, such as high strength-to-weight ratios. The material properties of a composite laminate depend on resin and fibre types and the ply orientations, resulting in highly tailorable structural designs. Composites are most notably used in the Boeing 787 Dreamliner and the Airbus A350 XWB, comprising around 80% of their structures by volume [1]. However, the use of composites in aircraft, especially carbon fibre reinforced polymers (CFRP), poses challenges in structural maintenance, as impact damage accumulated during service causes significant danger to structural safety [2]. CFRP laminates experience impact damage in aerospace applications due to dropped tools and chipped runways, causing local delamination, which can propagate under compressive loading and contribute to more severe buckling [3]. A commonly used mechanical test to determine impact-dependent properties is the compression after impact (CAI) test, as defined by the ASTM D7137/D7137M standard [4]. This test is used to investigate the residual compressive strength of a polymer matrix composite structure after damage by indentation using drop-weight impact testing.

Impact-damaged CFRP laminates exhibit non-uniform deformation properties due to local effects within the damaged area. Furthermore, the mechanical properties of CFRP laminates are often determined experimentally. Conventional engineering measurement techniques, such as strain gauges, provide strain measurements only at localized areas of a sample, while full-field strain mapping is necessary to measure the intricate strain patterns when the test sample is subjected to compressive loading. Three-dimensional digital image correlation (3D DIC) is an optical measurement technique that measures 3D strain and deformation at a full field of points over a singular sample.

3D DIC has been used in the investigation of full-field strain mapping of structures of a wide variety of sizes [5], and applications including characterizing deformations of membrane wings for micro air vehicles [6], [7], crack-tip behaviours of fracture specimens [8], [9], and the mechanical behaviour of super-pressure balloon structures [10]. The full-field measurement technique has also been used in studies on the 3D deformation behaviours of CFRP panels under CAI testing [11]–[14]. A study conducted by Rivallant et al. [11] used a 3D DIC system to investigate the out-of-plane displacement and buckling behaviours of laminates in both unidirectional and quasi-isotropic configurations. A study conducted by Tuo et al. [12] used a variety of measurement techniques, including 3D DIC, to investigate the out-of-plane displacement and axial strain fields in thin laminates. A study conducted by Wang et al. [13] used a 3D DIC system to investigate the out-of-plane displacement fields in three different laminates, distinguished primarily by the proportion of layer orientations. A study conducted by Sun et al. [14] used two 3D DIC systems. Both the front and back faces of CFRP panels were imaged to analyze 3D deformation behaviour under CAI testing. The study concluded that the 3D DIC measurements were highly applicable in validating quantitative numerical models that evaluated the impact damage tolerance of the composite structures.

In this work, large CFRP panels were subjected to various impact energy levels (0J, 30J, 3x 30J, 75J) in CAI testing. Varying boundary conditions were used, involving either inclusion or exclusion of additional support plates at each face of the panels. The 3D deformation behaviour of the panels was examined using a 3D DIC system imaging the front and back faces. This work focuses specifically on the findings for 75J impacted panels to demonstrate the imaging system and the visualization of the 3D DIC results. The objective of this work is to investigate the effects of boundary conditions on the deformation characteristics of the CFRP panels, such as out-of-plane displacement fields to determine local and global buckling, and axial strain fields to investigate the effects of the indentation caused by impact damage.

2 Methods

2.1 Sample Preparation

2.1.1 Sample Manufacturing

The CFRP laminate panels, shown in Figure 1, used in this study were manufactured from IM7/977-3 Carbon/Epoxy prepreg and had final dimensions of 254 mm x 304.8 mm x 4.3 mm (10” x 12” x 0.171”), shown in Figure 1(a). The panels had a layup configuration of $[0/45/90/-45]_{4s}$. A total of 13 panels were manufactured in pristine condition.

2.1.2 Installation of Strain Gauges

As shown in Figure 1(b), two-element 90° stacked rosette strain gauges (CEA-XX-062WT-350, Micro-Measurements, Wendell, NC) were installed to the panels at pre-defined locations. Results from the strain gauges were to be compared with the DIC measurements. Specifications of the biaxial strain gauges are listed in Table 1.

Table 1: Properties of biaxial strain gauges.

Property	Unit	Value
Gauge Factor	–	2.19
Nominal Resistance	Ω	350

2.1.3 Drop-Weight Impact Testing

The panels were subjected to drop-weight impact testing using a drop-weight system (Dynatup 8200, Instron, Norwood, MA), based on the ASTM D7136/D7136M standard [15], originally for 101.6 mm x 152.4 mm (4” x 6”)

panels, which was modified for the larger 254 mm x 304.8 mm (10” x 12”) panels. A hemispherical tip impactor with a diameter of 25.4 mm (1”) was used to impact a given sample at the designated impact energy level of 75J.

2.1.4 Surface Preparation and Painting

Surface preparation and painting were done to ensure effective DIC measurement. The panels were first cleaned throughout using ethanol to remove contaminants from the surfaces, thereby ensuring good uniformity and adhesion when applying a coat of paint. Next, a flat black base coat (Flat Black Spray Paint, Rust-Oleum, Concord, ON) was applied to the front and back surfaces, such that the surfaces had low reflectance for imaging.

A speckling pattern of paint (Opaque White 5212, Createx Colors, East Granby, CT) was applied to the front and back surfaces of the test panel, using an airbrush (H-SET, Paasche Airbrush Company, Chicago, IL). The pseudo-random pattern was achieved using a technique involving spraying the paint onto a disposable flat surface directed at the panel (i.e., a wooden tongue depressor), allowing large droplets of paint to form at the edges before they are sprayed onto the panel, creating a coarse stippling effect. The panel after preparation is shown in Figure 1. Figure 1(a) shows a CAD model of a panel with an illustrative speckle pattern texture applied to the surface. Figure 1(b) shows a physical example of a panel with a painted speckle pattern applied to the surface. Figure 1(c) shows the painted speckle pattern in an amplified view.

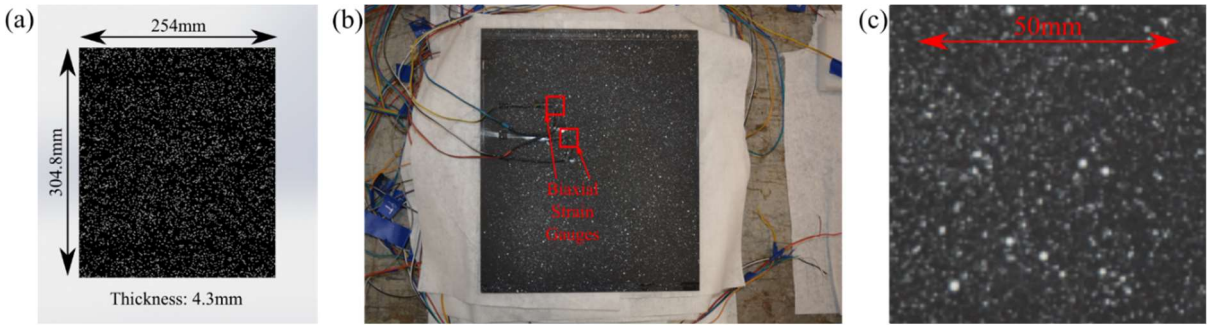

Figure 1: CFRP test panel: (a) schematic with dimensions and illustrative speckle pattern; (b) panel with mounted biaxial strain gauges; (c) amplified speckle pattern.

2.2 Imaging Setup

2.2.1 Imaging Setup at Panel Front and Back

A pair of high-resolution cameras (Ace acA2440-35um, Basler AG, Ahrensburg, Germany) was used for imaging of the front side of the sample. Each camera had a 50 mm fixed focal length lens (MVL50M23, Navitar, Rochester, NY) at an aperture size of f/11. Images were acquired at a rate of 5 frames per second for up to 180 seconds per test. The samples were illuminated using two continuous video lights (SL-60W CRI95+, Godox, Shenzhen, China).

A pair of high-resolution cameras (Imager M-Lite 5M, LaVision GmbH, Göttingen, Germany) was used for imaging of the back side of the sample. Each camera was equipped with a fixed focal length lens (35mm FL-CC3516-2M, RICOH, Düsseldorf, Germany) at an aperture size of f/11. Images were acquired at a rate of 5 frames per second for up to 180 seconds per test. Lighting to the region of interest was supplied by a pair of lights (Linear Illumination Unit 1103314, LaVision GmbH, Göttingen, Germany).

Camera and image properties for the standard-speed imaging systems are listed in Table 2. The full image acquisition setup is shown in Figure 2. Shown in Figure 2(a) and Figure 2(b), the cameras in the front-side imaging

system were mounted on a custom frame comprised of 95 mm aluminum extrusions (X95 Extrusions, Thorlabs, Newton, NJ) connected using corner cubes (XT95C1, Thorlabs, Newton, NJ) and sliding connections (XT95P13, Thorlabs, Newton, NJ). The cameras in the back-side imaging system were mounted on a tripod and rail (Strainmaster Mechanics 1103318, LaVision GmbH, Göttingen, Germany).

Table 2: Properties of standard-speed imaging setups.

Property	Unit	Value for Setup at Panel Front		Value for Setup at Panel Back	
		Added supports	*No added supports*	*Added supports*	*No added supports*
Camera Resolution	$px \times px$	2448 x 2048		2464 x 2056	
Pixel Size	μm	3.45		3.45	
Frame Rate	Hz	5		5	
Field of View	$mm \times mm$	138.3 x 115.7	317.9 x 266.0	183.9 x 153.4	183.9 x 153.4
Image Scaling Factor	px/mm	17.7	7.7	13.4	13.4
System Stereo Angle	° (deg)	25.9	18.9	18.7	18.7

2.2.2 Image Acquisition Timing and Synchronization

For imaging from the start of sample loading to the ultimate failure event, synchronization between the imaging systems at the front and back is crucial to accurately associate the 3D DIC results at both sides of the sample with the load and displacement data collected from the testing apparatus. Shown in Figure 2(c), system synchronization was achieved by incorporating a digital output voltage signal from a data acquisition (DAQ) device (USB 6210, National Instruments, Austin, TX). Using a MATLAB script, the Basler cameras were triggered using the Image Acquisition Toolbox, while digital data was sent to the DAQ device using the Data Acquisition Toolbox. The DAQ device then sends the rising edge +5V signal to the LaVision control unit, thereby triggering the LaVision cameras through DaVis 10 for image acquisition.

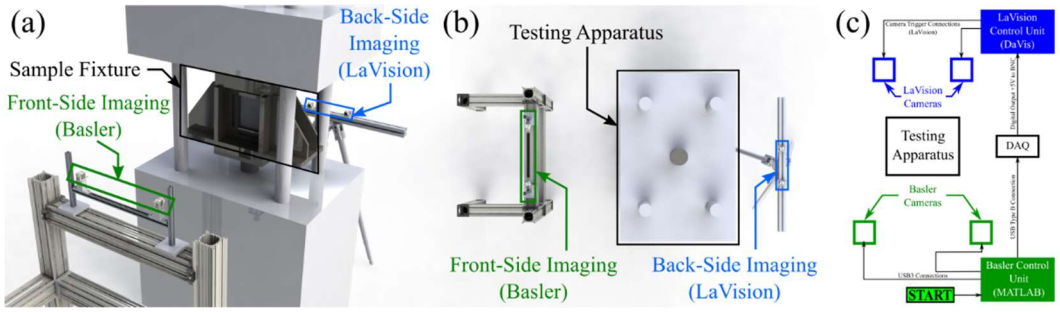

Figure 2: Full imaging and testing setup for CAI testing of CFRP panels: (a) isometric view for a panel with added supports; (b) top view with labelled systems; (c) wiring diagram for imaging and synchronization of front-side and back-side imaging systems.

2.3 Compression After Impact Testing

Compression after impact testing was performed using a servohydraulic test system with a load capacity of 1 MN (220 kips) (Model 311.31, MTS, Eden Prairie, MN, USA). Each panel was subjected to boundary conditions involving either only anti-buckling guides based on the ASTM D7137/D7137M standard [4], originally for 101.6 mm x 152.4 mm (4" x 6") panels, which was modified for the larger 254 mm x 304.8 mm (10" x 12") panels, or anti-buckling guides with added front and back support plates to reduce global buckling. The compression after impact fixture used in this study is shown in Figure 3.

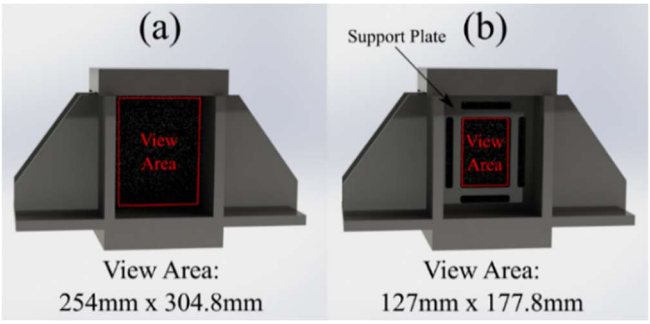

Figure 3: Compression After Impact fixture with (a) no added support plates; (b) added support plates.

The anti-buckling guides, shown in Figure 3(a), allowed the full 254 mm x 304.8 mm (10” x 12”) area of the panel to be visible for imaging. The added support plates, shown in Figure 3(b), limited the visible area to a central 127 mm x 177.8 mm (5” x 7”) area.

2.4 Data Acquisition

2.4.1 Load and Displacement Data Acquisition

During mechanical testing, the test system outputs voltages corresponding to the applied axial load and displacement. For each frame acquired by the LaVision cameras, these voltages were acquired through Bayonet Neill–Concelman (BNC) connections to the LaVision control unit and were then converted to loads using a scaling factor of 97.9 kN (22 kips) per volt, and displacements using a scaling factor of 12.7 mm (0.5”) per volt.

2.4.2 Strain Gauge Data Acquisition

Prior to testing, each uniaxial section of the strain gauges was wired in a separate quarter-bridge Wheatstone bridge configuration. During testing, an excitation voltage of 5 V was applied to each circuit, and the output voltage for each circuit was measured over time. The output voltage was then converted to strain using Equations (1) and (2), where V_0 denotes the initial measured voltage prior to testing, V denotes the measured voltage during testing, V_{Ex} denotes the applied excitation voltage, V_r denotes the voltage ratio, GF denotes the gauge factor of the strain gauge, R_L denotes the lead resistance, R_G denotes the nominal resistance of the strain gauge, and ε denotes the measured strain. For this analysis, since R_G was large, it was assumed that $R_L \ll R_G$.

$$V_r = \frac{V - V_0}{V_{Ex}} \qquad (1)$$

$$\varepsilon = -\frac{4V_r}{GF(1+2V_r)}\left(1+\frac{R_L}{R_G}\right) \qquad (2)$$

2.5 Image Processing

The compression test of the composite panels lasts 114 seconds without additional supports, and 83 seconds with additional supports. For each test, one in five frames were processed, generating measurements for 1 frame per second, which provides sufficient temporal resolution due to a low loading rate. Image pairs from each imaging system were processed, without pre-processing, using a commercial DIC software package (DaVis 10.0.3, LaVision GmbH, Göttingen, Germany), where 3D deformations and strains were evaluated at each frame. Each imaging system was calibrated using a two-level 3D calibration plate (Type 204-15, LaVision GmbH, Göttingen, Germany). A correlation was performed for each frame prior to failure, relative to the first frame of the test to prevent compounding precision errors. A subset size of 31 pixels and a step size of 10 pixels was used in the correlation procedure.

3 Results & Discussion

3.1 Out-of-Plane Displacement

The out-of-plane displacement results for the panels are shown in Figure 4. Figure 4(a) shows the out-of-plane displacement results for the panel with added supports, which reduce the unsupported area to 127 mm by 177.8 mm. The results indicate that the panel underwent an average out-of-plane displacement between 0.06 mm and 0.08 mm prior to entering a second (S-shaped) buckling mode and a maximum local out-of-plane displacement of about 0.4 mm prior to ultimate failure. From the averaged measurements shown in Figure 4(i), the panel deformed under a first (arc-shaped) buckling mode up to 60% failure load, where the bottom of the panel began to deflect in the opposite direction, as shown in Figure 4(ii). At 80% failure load, the panel is said to have fully transitioned to the second buckling mode. From the profiles shown in Figure 4(ii), local buckling of the impact-damaged area was evident at the back side of the panel, where the damage was applied, before 25% failure load was reached but extended towards the front side of the panel as 50% failure load was reached. Figure 4(b) shows the out-of-plane displacement results for the panel without added supports, resulting in a larger unsupported area of 254 mm by 304.8 mm. The results indicate that the panel underwent an average out-of-plane displacement of about 6 mm at the front side and about 9 mm at the back side, and a maximum local out-of-plane displacement of about 12 mm in a first buckling mode prior to ultimate failure. From the averaged measurements shown in Figure 4(iii), the panel experienced global buckling at the knee point of the curves after 40% failure load.

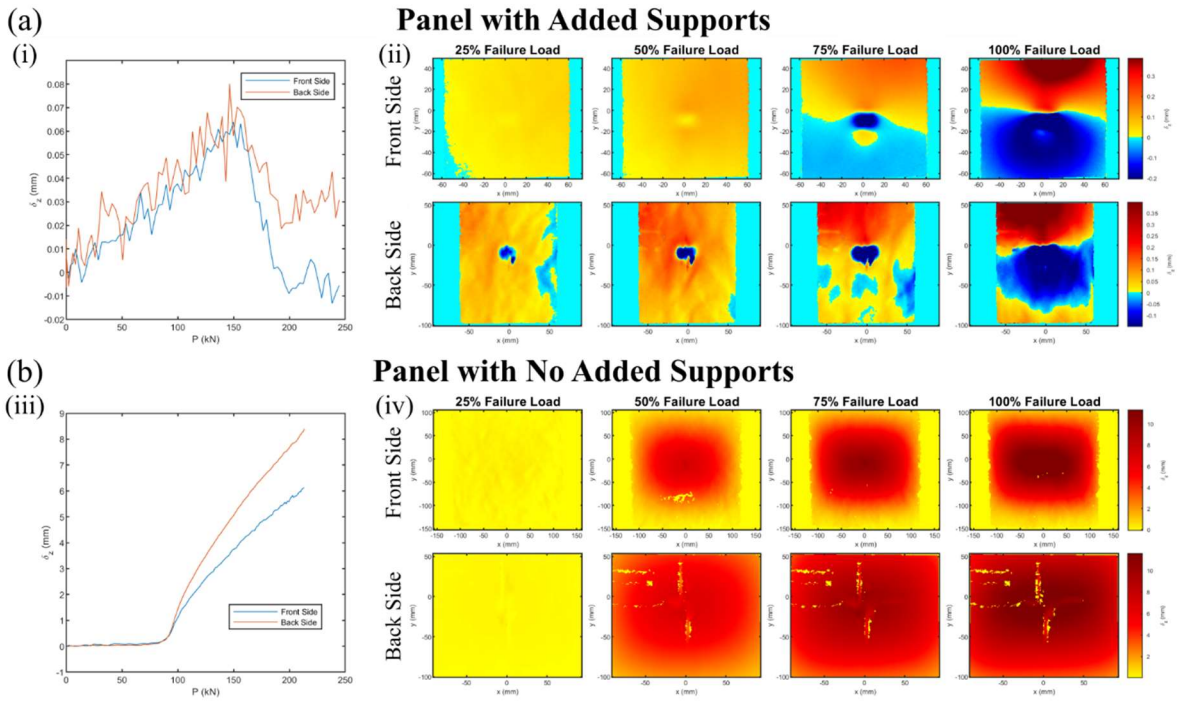

Figure 4: Out-of-plane displacement measurements for (a) the supported panel: (i) averaged values vs load; (ii) profiles; (b) the unsupported panel: (iii) averaged values vs load; (iv) profiles.

The DIC results from Sun et al. [14] indicated, for test panels with an unsupported area of 102 mm by 152 mm (4" by 6"), significant local buckling at the impact-damaged area and insignificant out-of-plane displacement occurred elsewhere. This observation correlates well with the results for the panel with added supports in this study. Results from Tuo et al. [12] indicated significant arc-shaped global buckling prior to ultimate failure. This observation correlates well with the results for the panel without added supports in this study. The DIC measurements in this

study therefore effectively demonstrate the effects of panel boundary conditions, characterized by the dimensions of the unconstrained area of the panel, on the presence of local and global buckling behaviours.

3.2 Axial Strain

The axial strain results for the supported and unsupported panels are shown in Figure 5. Figure 5(a) shows the axial strain results for the panel with added supports. The results indicate that the panel underwent a maximum compressive strain of about 0.6%, or 6,000 microstrain, prior to ultimate failure. From the averaged measurements shown in Figure 5(i), the panel experienced low global buckling, as the strain values have low deviation between the front and back sides of the panel. The progression of local buckling around the impact-damaged area is evident in the strain profiles shown in Figure 5(ii), similarly to the out-of-plane displacement profiles shown in Figure 4(ii), but the strain profiles provide a clearer perspective of the mechanism by which this local buckling occurs. In particular, the impact-damaged region experiences maximal compressive strain, while smaller neighbouring regions above and below the impact-damaged region experience low compressive strain. As the impact-damaged area buckles, it applies tension to the neighbouring regions to maintain the structural integrity of the panel. Figure 5(b) shows the axial strain results for the panel without added supports. The results indicate that the panel underwent a maximum compressive strain of about 1.4%, or 14,000 microstrain, prior to ultimate failure. From the averaged measurements shown in Figure 5(iii), the panel experienced significant global buckling, as the strain values between the front and back sides of the panel begin to diverge after 40% failure load. These results can be attributed to the introduction and development of bending strains caused by global buckling. Figure 4(b) indicates that the panel deflects towards the front-side imaging system, concluding the development of tensile bending strains at the front side of the panel and compressive bending strains at the back side of the panel. Figure 5(iii) confirms this conclusion, as the averaged measurements show significantly larger compressive strains at the back side of the panel than at the front side.

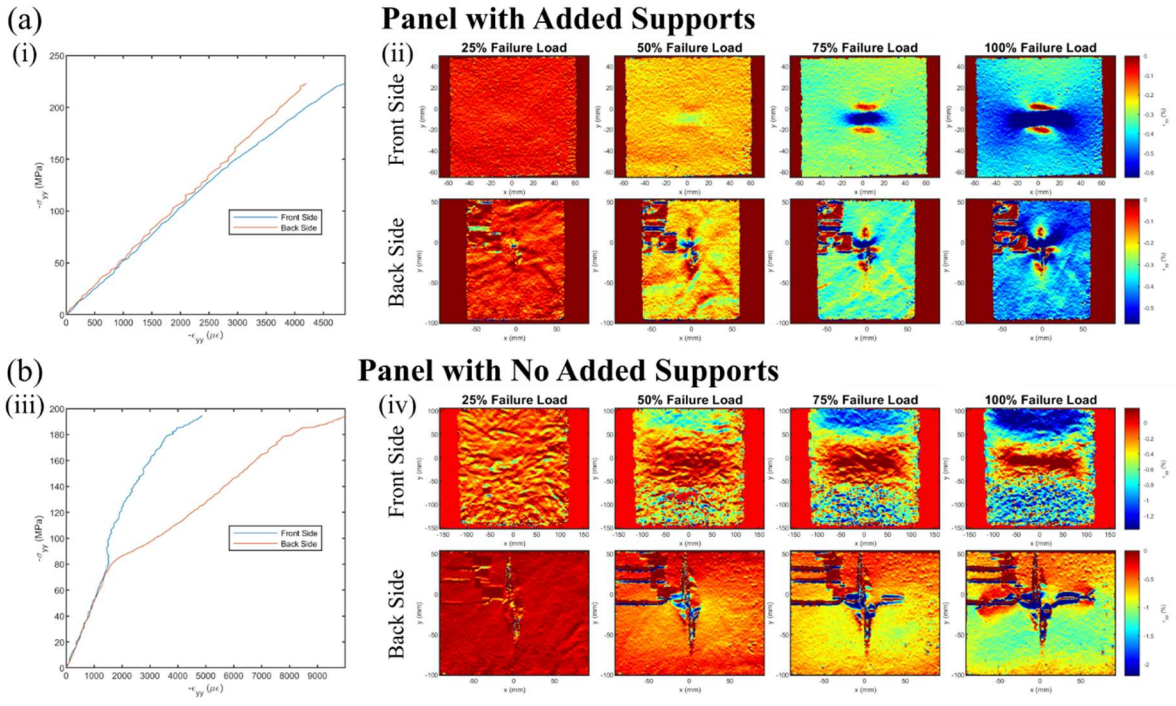

Figure 5: Axial strain measurements for (a) the supported panel: (i) compressive stress-strain curves from averaged values; (ii) profiles; (b) the unsupported panel: (iii) compressive stress-strain curves from averaged values; (iv) profiles.

Measurements for the back side of the panel notably include regions of outliers due to the presence of wires that are connected to the biaxial strain gauges. Since the wires have different deformation characteristics to the panel under the loading conditions, these regions are therefore excluded from the analysis. From the compressive stress-strain curves shown in Figure 5(i) and Figure 5(iii), the compressive modulus of elasticity of the panels can be measured. The compressive modulus of elasticity of each panel was estimated to be 54 GPa. The residual compressive strength was estimated to be 223 MPa and 194 MPa for the supported and unsupported panels, respectively.

3.3 Strain Gauge Measurements & DIC Data Error Analysis

The axial strain measurements from DIC were compared against measurements from the biaxial strain gauges for validation by error analysis. This process involves averaging DIC results over a small (7.5 mm x 7.5 mm) area, referred to as a "virtual strain gauge", then comparing the values against those measured by its corresponding biaxial strain gauge at the same loads. The virtual strain gauges, shown in Figure 6(i) and Figure 6(iv), were positioned at the back side of the panel, as closely as possible to a configuration mirrored to the biaxial strain gauges shown in Figure 1(b), and had a size of 11 x 11 subset steps (7.5 mm x 7.5 mm). The error analysis involves a procedure used in a study by Lava et al. [16], where the measurement difference $\Delta\varepsilon$, defined by Equation 3, for strain values $\varepsilon_{biaxial}$ and $\varepsilon_{virtual}$ measured by the biaxial and virtual strain gauges, respectively, is evaluated at each load. The mean absolute error $\Delta\varepsilon_{yy}$ is evaluated for a full test as the mean of the values of $|\Delta\varepsilon|$, and the standard deviation of differences σ is evaluated for a full test using the values of $\Delta\varepsilon$.

$$\Delta\varepsilon = \varepsilon_{biaxial} - \varepsilon_{virtual} \tag{3}$$

Figure 6(a) shows a comparison of the axial strain results between the biaxial and virtual strain gauges for the panel with added supports. Figure 6(b) shows a comparison of the axial strain results between the biaxial and virtual strain gauges for the panel without added supports.

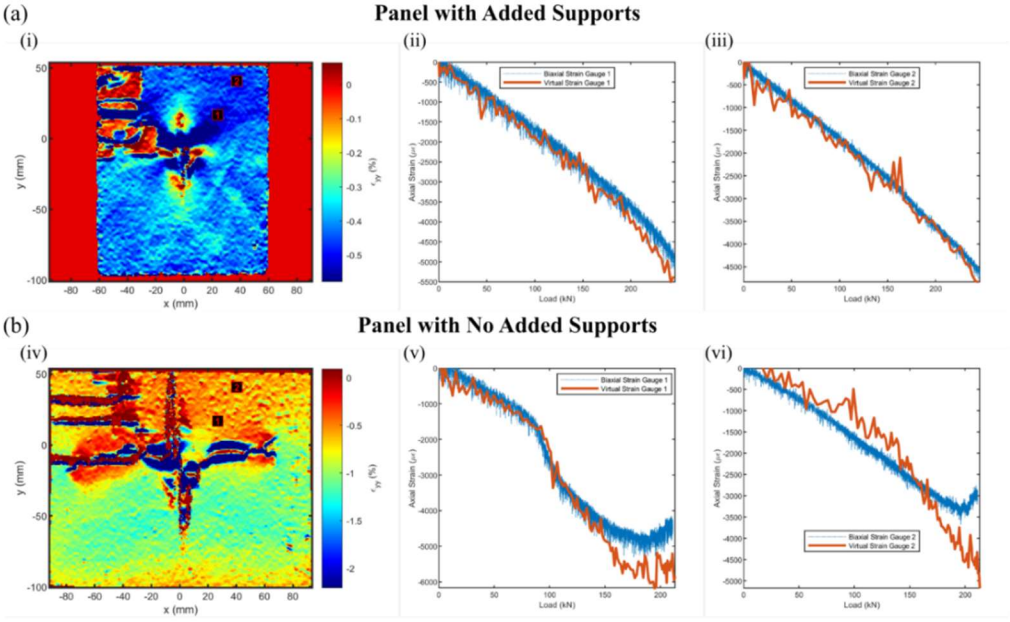

Figure 6: Comparison of axial strain measurements for (a) the supported panel: (i) profile plot with labelled virtual strain gauges; (ii) axial strain vs load for biaxial and virtual strain gauge 1; (iii) axial strain vs load for biaxial and virtual strain gauge 2; (b) the unsupported panel: (iv) profile plot with labelled virtual strain gauges; (v) axial strain vs load for biaxial and virtual strain gauge 1; (vi) axial strain vs load for biaxial and virtual strain gauge 2.

The error estimation study performed by Lava et al. [16] provides results for 3D DIC measurement of highly ductile sheet metal specimens under tensile loading, using a set of images generated using finite element (FE) displacement fields, as well as a set of images acquired for an experimental case. The numerical results for the stereo angle corresponding to the back-side imaging system are $\Delta\varepsilon_{yy} = 300\ \mu\varepsilon$ and $\sigma = 7000\ \mu\varepsilon$, while the experimental results are $\Delta\varepsilon_{yy} = 221\ \mu\varepsilon$ and $\sigma = 1850\ \mu\varepsilon$ [16].

For the supported panels, the mean absolute errors are near the experimentally determined "expected value" of $\Delta\varepsilon_{yy} = 221\ \mu\varepsilon$ [16], but for the unsupported panels, the mean absolute errors are significantly larger. This conclusion is attributed to the different loading conditions between this work, which examines compressive deformation that causes buckling and high out-of-plane tilting of the sample, and the error estimation study by Lava et al. [16], which examines tensile deformation where out-of-plane tilting of the sample is negligible. Shown in Figure 6(vi), for virtual strain gauge 2, the compressive strains are underestimated at lower loads, which can be attributed to the positioning of the virtual strain gauge, as the biaxial strain gauge was located above the area measured by DIC. Shown in Figure 6(v) and Figure 6(vi), both virtual strain gauges overestimate the compressive strains at higher loads, which can be attributed to a high tilt angle of the panels at these positions. The biaxial strain gauges provide measurements based on a coordinate system dependent on the local orientation of the panel, while the virtual strain gauges provide measurements based on a fixed coordinate system dependent only on the imaging system. Consequently, results from DIC measurements are acceptable when compared with results from strain gauge measurements only in situations where the strain gauge remains normal to the out-of-plane axis of DIC measurement, as out-of-plane tilt would cause an increase in measured compressive strain with respect to the fixed coordinate system in DIC.

Conclusions

Compressive 3D deformation properties were investigated in CAI testing of CFRP panels under various boundary conditions, where full-field optical measurement using 3D DIC at each face (front and back) of the panel was demonstrated. This work examined cases for panels with 75J of impact energy and is part of a larger study that also examines other impact energy levels (no impact damage, 30J, and 30J three times). Measurements of out-of-plane displacement demonstrated the occurrences and modes of local and global buckling. Measurements of axial strain demonstrated the global strain behaviours, as well as the effects of the impact-damaged region on the local strain behaviours in neighbouring regions, and allowed for estimation of material properties such as compressive modulus of elasticity and residual compressive strength. A comparison of virtual strain gauges derived from DIC measurements with biaxial strain gauges demonstrated, where local panel tilt is low and the position of the virtual strain gauge is accurate, measurement errors near the experimental expected value of 221 microstrain and below the numerical expected value of around 300 microstrain. This method can therefore be applied to assess deformation and strain behaviours of CFRP panels subject to a range of impact damage levels**.**

References

[1] V. Giurgiutiu, "Chapter 1 - Introduction," in *Structural Health Monitoring of Aerospace Composites*, V. Giurgiutiu, Ed. Oxford: Academic Press, 2016, pp. 1–23. doi: https://doi.org/10.1016/B978-0-12-409605-9.00001-5.

[2] J. López-Puente, R. Zaera, and C. Navarro, "Experimental and numerical analysis of normal and oblique ballistic impacts on thin carbon/epoxy woven laminates," *Composites Part A: Applied Science and Manufacturing*, vol. 39, no. 2, pp. 374–387, Feb. 2008, doi: 10.1016/J.COMPOSITESA.2007.10.004.

[3] A. T. Rhead, R. Butler, and G. W. Hunt, "Compressive strength of composite laminates with delamination-induced interaction of panel and sublaminate buckling modes," *Composite Structures*, vol. 171, pp. 326–334, Jul. 2017, doi: 10.1016/J.COMPSTRUCT.2017.03.011.

[4] "ASTM D7137/D7137M-17 Standard Test Method for Compressive Residual Strength Properties of Damaged Polymer Matrix Composite Plates," in *Annual Book of ASTM Standards*, vol. 15.03, 2017.

[5] M. A. Sutton, J.-J. Orteu, and H. W. Schreier, "Introduction," in *Image Correlation for Shape, Motion and Deformation Measurements: Basic Concepts, Theory and Applications*, Boston, MA: Springer US, 2009, pp. 1–12. doi: 10.1007/978-0-387-78747-3_1.

[6] B. Stanford, R. Albertani, and P. Ifju, "Static finite element validation of a flexible micro air vehicle," *Experimental Mechanics*, vol. 47, no. 2, pp. 283–294, Apr. 2007, doi: 10.1007/s11340-006-9003-y.

[7] A. H. Wrist and J. P. Hubner, "Aerodynamic comparisons of flexible membrane micro air vehicle wings with cambered and flat frames," *International Journal of Micro Air Vehicles*, vol. 10, no. 1, pp. 12–30, Mar. 2018, doi: 10.1177/1756829317705327.

[8] P. F. Luo, Y. J. Chao, M. A. Sutton, and W. H. Peters, "Accurate measurement of three-dimensional deformations in deformable and rigid bodies using computer vision," *Experimental Mechanics*, vol. 33, no. 2, pp. 123–132, 1993, doi: 10.1007/BF02322488.

[9] P. F. Luo and F. C. Huang, "Application of stereo vision to the study of mixed-mode crack-tip deformations," *Optics and Lasers in Engineering*, vol. 33, no. 5, pp. 349–368, 2000.

[10] P. Vialettes *et al.*, "Experimental and numerical simulation of super-pressure balloon apex section: Mechanical behavior in realistic flight conditions," *Advances in Space Research*, vol. 37, no. 11, pp. 2082–2086, 2006, doi: 10.1016/j.asr.2005.04.064.

[11] S. Rivallant, C. Bouvet, E. Abi Abdallah, B. Broll, and J. J. Barrau, "Experimental analysis of CFRP laminates subjected to compression after impact: The role of impact-induced cracks in failure," *Composite Structures*, vol. 111, no. 1, pp. 147–157, 2014, doi: 10.1016/j.compstruct.2013.12.012.

[12] H. Tuo, Z. Lu, X. Ma, J. Xing, and C. Zhang, "Damage and failure mechanism of thin composite laminates under low-velocity impact and compression-after-impact loading conditions," *Composites Part B: Engineering*, vol. 163, pp. 642–654, Apr. 2019, doi: 10.1016/j.compositesb.2019.01.006.

[13] X. Wang, J. Huang, R. Tan, Y. Su, Z. Guan, and X. Guo, "Experimental investigation on damage mechanisms and buckling behaviors of thin composite laminates in compression after impact," *Composite Structures*, vol. 256, Jan. 2021, doi: 10.1016/j.compstruct.2020.113122.

[14] X. C. Sun and S. R. Hallett, "Failure mechanisms and damage evolution of laminated composites under compression after impact (CAI): Experimental and numerical study," *Composites Part A: Applied Science and Manufacturing*, vol. 104, pp. 41–59, Jan. 2018, doi: 10.1016/j.compositesa.2017.10.026.

[15] "ASTM D7136/D7136M-20 Standard Test Method for Measuring the Damage Resistance of a Fiber-Reinforced Polymer Matrix Composite to a Drop-Weight Impact Event," in *Annual Book of ASTM Standards*, vol. 15.03, 2020.

[16] P. Lava, S. Coppieters, Y. Wang, P. van Houtte, and D. Debruyne, "Error estimation in measuring strain fields with DIC on planar sheet metal specimens with a non-perpendicular camera alignment," *Optics and Lasers in Engineering*, vol. 49, no. 1, pp. 57–65, Jan. 2011, doi: 10.1016/j.optlaseng.2010.08.017.